

# Breaking the temporal and frequency congestion of LiDAR by parallel chaos

Received: 19 May 2022

Accepted: 12 January 2023

Published online: 13 March 2023

 Check for updatesRuixuan Chen<sup>1,4</sup>, Haowen Shu<sup>1,4</sup>, Bitao Shen<sup>1,4</sup>, Lin Chang<sup>1,2,3,4</sup>✉, Weiqiang Xie<sup>2</sup>, Wenchao Liao<sup>1</sup>, Zihan Tao<sup>1</sup>, John E. Bowers<sup>2</sup>✉ & Xingjun Wang<sup>1,3</sup>✉

The rising demand for high scanning accuracy and resolution in sensors for self-driving vehicles has led to the rapid development of parallelization in light detection and ranging (LiDAR) technologies. However, for the two major existing LiDAR categories—time-of-flight and frequency-modulated continuous wave—the light sources and measurement principles currently used for parallel detection face severe limitations from time- and frequency-domain congestion, leading to degraded measurement performance and increased system complexity. In this work we introduce a light source—the chaotic microcomb—to overcome this problem. This physical entropy light source exhibits naturally orthogonalized light channels that are immune to any congestion problem. Based on this microcomb state, we demonstrate a new type of LiDAR—parallel chaotic LiDAR—that is interference-free and has a greatly simplified system architecture. Our approach also enables the state-of-the-art ranging performance among parallel LiDARs: millimetre-level ranging accuracy and millimetre-per-second-level velocity resolution. Combining all of these desirable properties, this technology has the potential to reshape the entire LiDAR ecosystem.

LiDAR technology has undergone remarkable advances over the past few years, driven by the interest in autonomous vehicles<sup>1–4</sup>. Safe, reliable unmanned driving can only be achieved through real-time updates of three-dimensional (3D) information of the surrounding environments in a wide field of view and with high imaging resolution. To achieve this goal, one major evolutionary route of LiDAR is parallelization<sup>5</sup>: by conducting multichannel measurements simultaneously, 3D imaging can be realized with only 1D scanning, leading to a substantially improved acquisition rate and angle resolution. Moreover, parallelization can also relieve the reliance on the beam-steering mechanism. Commercial LiDAR currently carries up to 128 channels for parallel detection<sup>6</sup>.

However, despite these advantages, the previously developed parallel LiDARs all face a critical challenge in channel congestion (see Fig. 1a,b): the overlap between light channels in the time or frequency

domain makes it difficult to distinguish the effective echo signals from interference. Pulsed laser sources are used for time-of-flight (TOF) LiDAR and the temporal congestion comes from the interference between adjacent channels or other external pulsed sources mixing with the valid channel echo signal<sup>7</sup>; coherent frequency lines serve as the light source for the recently demonstrated parallel frequency-modulated continuous-wave (FMCW) LiDAR<sup>8</sup>, and any frequency domain overlaps—whether from other signal lines on the same source or from another coherent light source<sup>9</sup>—will cause frequency congestion. Such congestion usually results in degraded ranging accuracy or fake images<sup>7</sup>, which are becoming a major problem for LiDAR's development, particularly when multiple devices work within a limited space—a common working scenario for self-driving vehicles. Moreover, it is foreseeable that the external space on the future road

<sup>1</sup>State Key Laboratory of Advanced Optical Communications System and Networks, School of Electronics, Peking University, Beijing, China. <sup>2</sup>Department of Electrical and Computer Engineering, University of California, Santa Barbara, CA, USA. <sup>3</sup>Frontiers Science Center for Nano-optoelectronics, Peking University, Beijing, China. <sup>4</sup>These authors contributed equally: Ruixuan Chen, Haowen Shu, Bitao Shen, Lin Chang. ✉e-mail: [linchang@pku.edu.cn](mailto:linchang@pku.edu.cn); [bowers@ece.ucsb.edu](mailto:bowers@ece.ucsb.edu); [xjwang@pku.edu.cn](mailto:xjwang@pku.edu.cn)

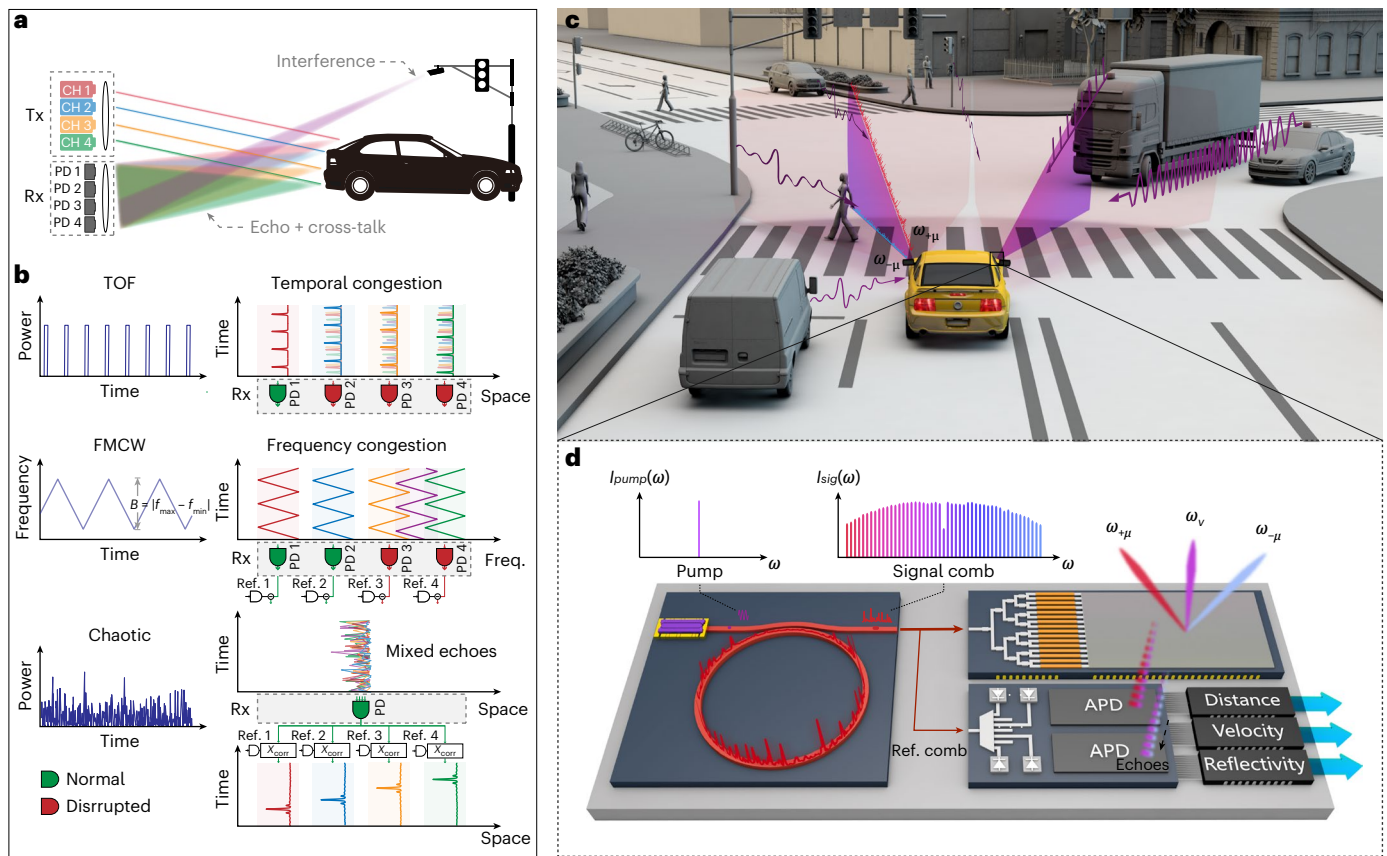


**Fig. 1 | A congestion-free LiDAR by parallel chaos. a,** Scenario illustration of the congestion detector.  $T_x(R_x)$  represents the transmitter (Receiver); PD represents the photodetector;  $B$  represents the bandwidth of the linear frequency chirp, while  $f_{max}$  and  $f_{min}$  denote the maximum and minimum frequency. **b,** Comparisons between the parallel TOF, FMCW and chaotic LiDAR show the advantages of using parallel chaos, which includes breaking the temporal and frequency congestion and system simplicity in the receiving end. **c,** Conceptual diagram of the parallel chaotic LiDAR used in a real scenario. **d,** Conceptual illustration of

integrated parallel LiDAR system, which is mounted in the headlight position of the car shown in **c**. The chaotic comb with a wide spectrum range is pumped by a heterogeneous integrated DFB laser and is emitted to different spatial channels in correspondence with the wavelength of the comb line by a one-dimensional optical phased array (OPA). The echoes containing all wavelength channels are received simultaneously by two high-sensitivity PDs and calculated with the demultiplexed reference channels to obtain the distance, velocity and reflectivity information by Application Specific Integrated Circuits.

will be flooded with different types of LiDAR signals, and the probability of interference between LiDARs will increase considerably, as indicated in Fig. 1c.

The wisdom from other fields that use parallel information processing can be employed to overcome this problem: in wireless communications, the code-division multiple-access systems<sup>10</sup> are able to arrange each user with a unique and quasi-orthogonal coding sequence, thereby improving spectrum efficiency and reducing inter-channel cross-talk. Likewise, in radar technologies, multi-input multi-output radar systems transmit mutually orthogonal signals from multiple transmit antennas, and these waveforms can be extracted from each of the receive antennas by a set of matched filters<sup>11–13</sup>. However, the implementation of such strategies in LiDAR technology is much more challenging: although orthogonal coding of the light source<sup>14</sup> can help alleviate the interference problem<sup>15–17</sup>, digital LiDARs based on pseudo-random modulation<sup>18</sup> require high-speed optoelectronics for pattern generation and modulation; the chaotic LiDAR is proposed to generate chaos-modulated light by using intrinsic laser dynamics<sup>19</sup>, which can eliminate the additional power consumption for orthogonal coding<sup>20–22</sup>, but the generation of chaotic waveforms still requires careful external feedback. Besides, both approaches have faced the same problem of limited detection throughput due to the long accumulation time window for each probe test, which makes them unsuitable for real-time high-speed 3D imaging<sup>23</sup>. Overall, the lack of manner

to effectively generate parallel chaotic signals in an energy-efficient and low-cost way hinders further evolution of high-speed LiDAR with strong resistance to interference/jamming. Moreover, the ranging information of chaotic LiDAR is extracted from the correlation between the reference and echo signals, and the detection accuracy directly depends on the bandwidth of the modulation<sup>24</sup>. To satisfy the high precision requirement in self-driving vehicles and other applications, high-speed random number generators and electro-optical modulators are necessary, which pose a substantial increase in cost and system complexity for parallelization. These difficulties, combined with the challenges of high-level photonic integration of LiDAR systems, have been stalling the progression of this field.

In this work we break through the temporal and frequency congestion barriers by introducing a novel electromagnetic wave source—chaotic microcombs—to ranging and detection systems. Induced by the instability of a Kerr microresonator pumped by a continuous-wave laser, the special comb state exhibits an inherently spatial-temporal chaotic nature, where every comb line is orthogonal and therefore can be clearly distinguished from every other comb line even when they overlap in both the time and frequency domains. Based on such a chaotic light source, we demonstrated a parallel chaotic LiDAR system that is immune to interference. By using a highly nonlinear AlGaAsOI microresonator, a record-high chaotic spectrum beyond 12 GHz for microcombs has been demonstrated, which leads to an

unprecedented ranging precision of 2 mm and accurate velocity detection of a slow-moving (<5 millimetre-per-second speeds) target. We also present a high-resolution 3D image by using 51 comb lines. Due to the desirable properties of chaos-endowed orthogonality, the architecture for such high-level parallelization is very simple (shown in Fig. 1d): only a single source is used at the transmitter side and only two photodetectors are required at the receiver side without any multiplexing components, which greatly reduce the system's cost. Importantly, all of the components in the architecture are integration compatible, which provides the technical basis for future high-volume-produced wafer-scale LiDARs. Furthermore, this chaotic LiDAR shows outstanding interference tolerance: a reasonable SNR can still be attained when the interference light is 1,000-times stronger than detection signals received at the photodetector. With these results, our work demonstrates a new solution to high-performance and low-cost LiDAR, and similar parallelization-based strategies can be further extended to a much broader electromagnetic spectrum such as radar, millimetre-wave and terahertz-wave systems.

### Parallel chaos generated by microcombs

In this work, the parallel chaos is generated by continuous-wave pumping an AlGaAsOI (refs. <sup>25,26</sup>) microresonator, as shown in Fig. 2. The waveguide dimension of the resonator is 600 nm × 400 nm, ensuring anomalous dispersion in the C band. By manually tuning the frequency of the pump laser into a resonance around 1,550 nm, a chaotic microcomb can be generated without any feedback or control circuitries. As shown in Fig. 2b, the chaotic comb has a trapezoid envelope, with an ultra-flat spectrum in the central part.

The key difference of such a chaotic state, compared with the commonly used coherent soliton microcombs<sup>27</sup>, is the inherently chaotic nature: all comb lines bear random intensity and frequency modulations. This property is characterized by sending each comb line into a photon detector. As an example, we picked one comb line generated from a 90 GHz resonator (labelled in Fig. 2b) and plotted its properties in Fig. 2c–e. It can be found that the amplitude randomly fluctuates temporally, resulting in chaotic behaviour (Fig. 2c). Its autocorrelation function (ACF) is plotted in Fig. 2d, which shows a delta-function shape, preventing possible range ambiguity from self-interference<sup>28</sup>. Importantly, as every comb line is orthogonal to each other (the only exception is the correlated relationship between pair of comb lines symmetric to the pump due to the nature of the parametric oscillation process), the congestion problems of signals in temporal and frequency domains can be completely lifted.

In chaotic LiDAR measurement, the ranging accuracy is directly related to the range resolution  $R$  by

$$R = \frac{c \times \text{FWHM}}{2} \quad (1)$$

where  $c$  is the velocity of light, and FWHM is the full-width at half-maximum of the ACF. As governed by the Kerr effect, the chaotic dynamic is directly determined by the nonlinear coefficient and intracavity energy density. One key advantage of this work is the use of the AlGaAsOI platform for generating the chaotic comb state. The giant Kerr nonlinear coefficient of AlGaAs, which is the highest among commonly used integrated photonic media, enables an FWHM of lower than 0.15 ns, which corresponds to a range resolution of ~2.25 cm. Such resolution is comparable with state-of-the-art LiDAR technologies. Reflected in the chaotic spectrum, Fig. 2e shows the radio frequency spectrum for the generated chaos over a broad frequency range up to 7 GHz. The chaotic spectrum can be further expanded by pumping a smaller ring for a higher energy density. Figure 2e also shows the radio frequency spectrum of chaotic combs generated in the 850 GHz ring. A wider chaotic spectrum up to 12 GHz can be obtained by using a smaller ring, which suggests an even higher range resolution.

The high range resolution and chaotic spectrum make AlGaAsOI a superb choice over other material platforms in terms of generating a chaotic microcomb state. In Fig. 2f we simulate the range resolution based on chaotic combs generated in the commonly used microcomb platforms. At the same power level, the chaotic state in AlGaAsOI produces one order of magnitude better resolution than the most widely used Si<sub>3</sub>N<sub>4</sub> microcomb. Based on the calculation, a range resolution down to 3 cm is available with ~20 dBm pump power when using the 90 GHz AlGaAsOI microcomb, consistent with our experimental result. The pump power level can be achieved by an on-chip laser or semiconductor optical amplifier, which makes this approach desirable for future full integration while maintaining great performance.

The detuning between the pump laser and cavity resonance is a critical parameter that affects the chaotic nature of the comb state. In Fig. 2g we estimate the range resolution under different detuning of 51 comb lines in the C band by measuring FWHMs. The chaotic state can be maintained within a 50 GHz detuning range. The range resolutions <3 cm for all comb lines in the C band are ensured in an 18 GHz detuning range. Typically, the long existence range results from a combination of the Kerr shift and thermal resonance shift<sup>29,30</sup>. In the AlGaAsOI platform, the ultra-long existence range of the chaotic comb state is attributed to the high thermo-optical effect, as detailed in Supplementary Note 1. The ultra-long existence range promises a stable free-running source, which is vital for practical applications, unlike with the above-demonstrated parallel FMCW LiDAR, whose light source is a soliton state and requires complicated control and feedback in operation.

### Non-cross-talk, high-precision parallel ranging

Harnessing this novel light source, here we demonstrated a new type of LiDAR: the parallel chaotic LiDAR. The principle of chaotic ranging is based on the correlation property of the random intensity-modulated signal. By calculating the cross-correlation between the signal and reference, the delay time of the launching signal taking in the round-trip of free space can be obtained from the position of the correlation peak, thereby determining the distance.

The naturally parallel chaos can offer a more simplified architecture than previous parallel LiDARs: at the transmitter side, the massive number of mutually orthogonal channels are generated simultaneously by just pumping the AlGaAsOI microresonator by a continuous-wave laser. The large accessing window of such a chaotic state helps get rid of all of the optical and electronic control circuitries while still maintaining the consistency and stability of the comb state; at the receiver side, the chaos-endowed orthogonality naturally isolates each channel, therefore supporting single-pixel detection<sup>31</sup> for a group of parallel echo signals. The signal of the target channel is then distinguished from the mixture of multichannel echoes by a simple cross-correlation calculation. As channels are highly orthogonal with each other, the cross-correlation between the reference and unmatched channel will be zero and only the target channel will show a correlation peak. Such a scheme greatly relieves the number of receiving photodetectors, which was a major expense when doing all kinds of parallelization in previous LiDAR technologies. Although a photodetector array must be employed at the reference end in this scheme, the array does not need to be highly responsive and sensitive due to the much higher signal power than that at the receiver end, therefore leading to much lower cost.

Here we experimentally characterized the proposed parallel chaotic LiDAR system with non-cross-talk and high-precision ranging. In the set-up shown in Fig. 3a, an amplified continuous-wave laser was used as a pump to generate the chaotic comb. A total of 20 comb lines between 1,543 nm and 1,558 nm were selected for ranging characterization, half of which fell to the left side of the pump and the other half to the right. As the four-wave mixing process that excites the Kerr comb leads to a stronger correlation between the pump-centered symmetrical comb pairs, two detectors are required to receive the echoes from the corresponding single-sided combs. In the experiment, ten comb lines are



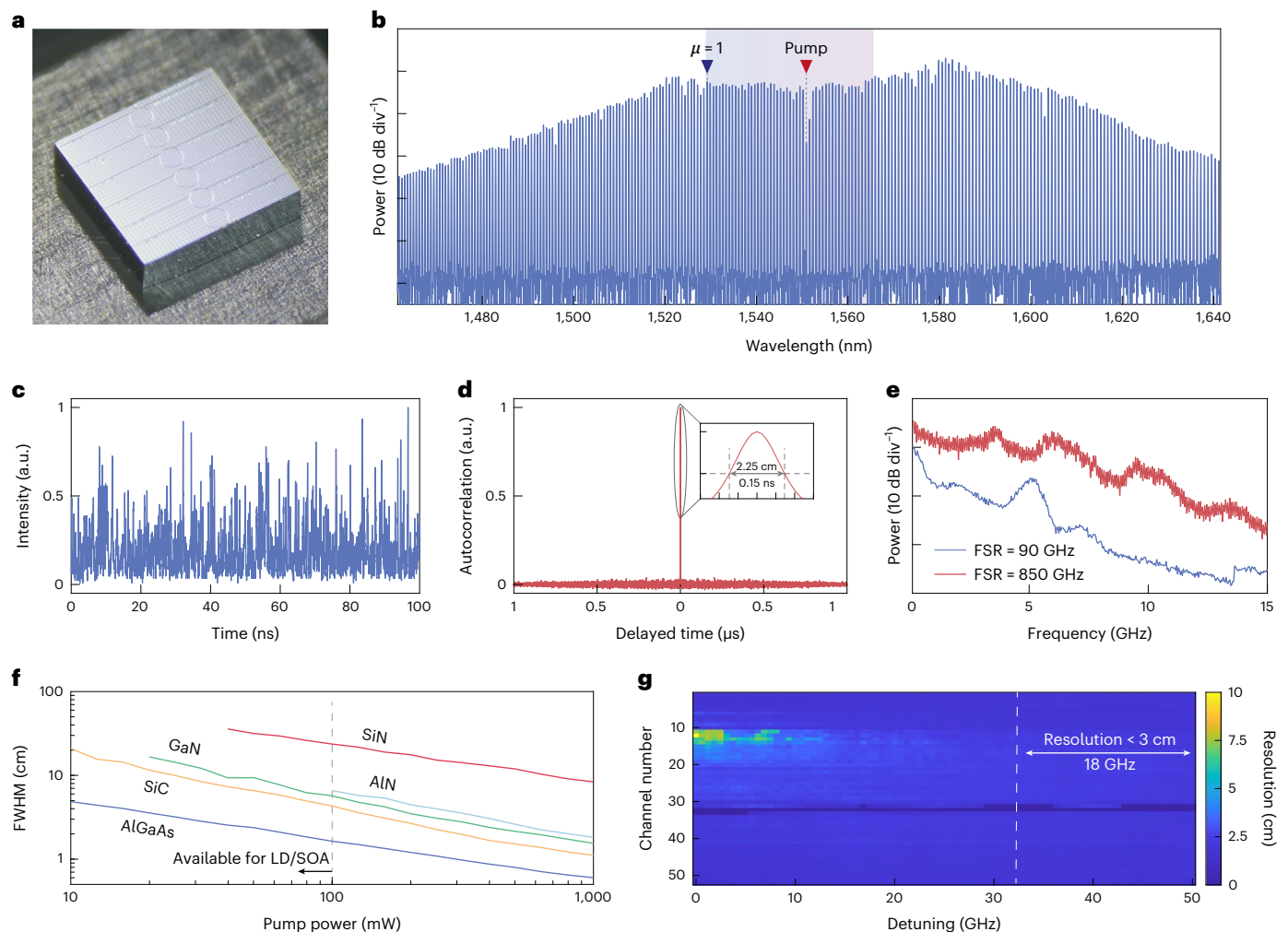


**Fig. 2 | Generation of the parallel chaos by chaotic microcombs. a**, Optical micrograph of the AlGaAsOI chip for ring resonators with a free spectral range of 90 GHz. **b**, The optical spectrum of the generated chaotic comb with the on-chip pump power of -130 mW. The pump, marked by the red arrow, is suppressed by a fibre Bragg grating (FBG). The blue shading indicates comb lines in the C band. **c–e**, The temporal waveform (**c**), the autocorrelation function (**d**) and the radio frequency spectrum (**e**) of the first comb line in the C band marked

by the blue arrow in **b** with  $\mu$  denoting the label of the comb line. The inset in **d** is the magnified autocorrelation function. **f**, The simulated range resolution for different integrated nonlinear platforms with different pump powers, see Methods for more details. **g**, Experimentally estimated range resolutions of 51 comb lines in the C band under different detuning. The dark blue region for channel numbers around 32 indicates comb lines suppressed by the FBG.

launched at a time and dispersed by a transmission grating into the free space to detect different points on a whiteboard (see Supplementary Note 2). Meanwhile, the comb is power split, demultiplexed and then fed into the reference photodetectors. The spectral echoes scattered from the target object were amplified and received without demultiplexing. As shown in Fig. 3b, the correlation calculation is performed channel by channel, and then the detected distance of the specific channel  $x_\mu$  can be derived from the lag time of the correlation peak  $\Delta t_\mu$  by

$$x_\mu = \frac{c \times \Delta t_\mu}{2} \quad (2)$$

Figure 3c shows the SNR of the correlation peak and average distance result for each ranging channel. The spectral non-uniformity of the SNR of the correlation peaks comes from the irregular reflections from the uneven surface of the whiteboard. Although the decreased SNR may result in deviations in the delay time, it can be resolved by averaging the results of multiple detections. The ranging results of all channels exhibit high consistency, which verifies that the proposed parallel chaotic LiDAR system permits simultaneous demodulation of spectral

echoes with a simplified system structure and no channel-to-channel cross-talk. Our parallel ranging demonstration's excellent immunity to inter-channel interference is of great potential because the number of high-performance detectors does not increase substantially as the number of parallel channels increases, which can greatly reduce the cost at the receiving end due to the increased detection throughput. Furthermore, the performance of existing on-chip high-speed germanium detectors is sufficient to meet the needs of the reference end and is capable of large-scale integration. Such a scheme that requires only one photodetector at the receiving end to achieve multiwavelength channel detection was previously implemented via a time-stretching method<sup>32</sup> and spectro-temporal encoding<sup>33</sup>. By contrast, our scheme is able to detect parallel channels simultaneously without consuming additional hardware or modulation power at the transmitter side.

To verify the capability of high-precision ranging offered by the broad chaotic spectrum discussed in the last section, we selected one channel whose chaotic spectrum was beyond 12 GHz for whiteboard detection. The motorized target was set to move along the rail and away from the collimator in steps of 1 cm, and then the corresponding distance between the collimator and target was measured. Figure 3d

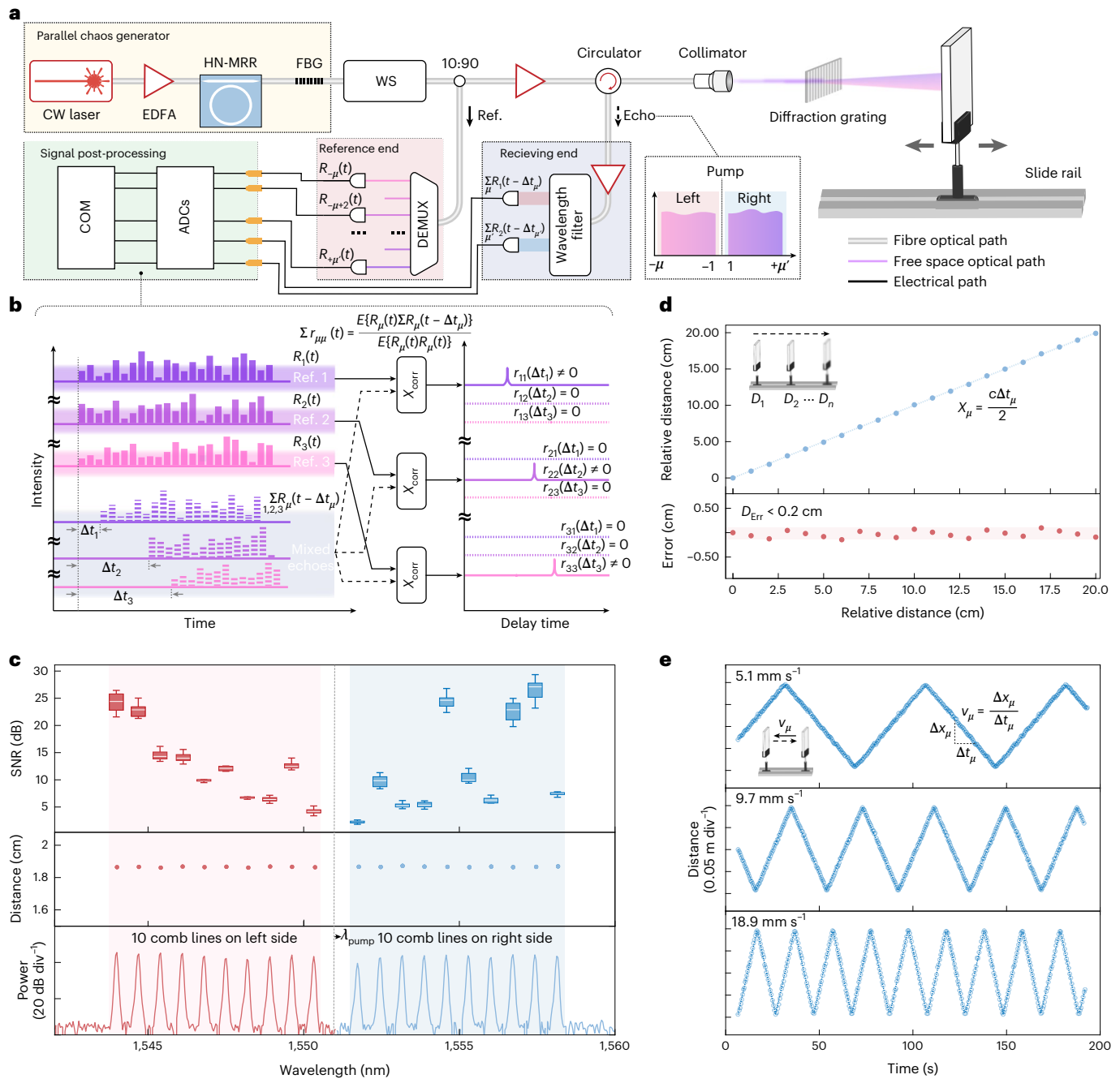


**Fig. 3 | Non-cross-talk and high-precision parallel ranging.** **a**, Experimental set-up of the parallel ranging based on chaotic microcomb. The multiple comb lines with naturally temporal orthogonality are launched by the collimator and the horizontal positions on the target are mapped to wavelength channels through the dispersion of a 966 lines per millimetre transmission grating. The filter range of the FBG is 1 nm with the pump wavelength in the centre of the filtering passband. HN-MRR, highly nonlinear microring resonator; WS, waveshaper; CW, continuous wave; EDFA, erbium-doped optical fiber amplifier; DEMUX, demultiplexer; ADC, analog-to-digital converter; COM, computer. **b**, The principle illustration of the correlation processing using the mixed echoes and references in signal post-processing shown in **a**. Three channels ( $R_1$ ,  $R_2$  and  $R_3$ ) are shown in this example for simplicity. Different colours indicate the three separate channels in the reference end and the mixed echoes in the receiving end.

$r_{\mu\nu}$  represents the cross-correlation between reference channel  $\mu$  and component from channel  $\nu$  in the receiving mixed echoes.  $D_n$  denotes the measured distance of the  $n$ th test;  $v_{\mu}(X_{\mu})$  denotes the velocity (relative distance) measured by channel  $\mu$ . **c**, Distance measurement results of parallel ranging, with ten channels demodulated at the same time. The spectral echo signals are isolated, amplified and directed to a single receiving photodetector without the need for demultiplexing. The box plots are derived from the number of tests ( $N = 10$ ), respectively. The horizontal line indicates the median, the box spans the 0.25 to 0.75 quartiles and the whisker length corresponds to 1.5 times the interquartile range. **d**, Characterization of the ranging accuracy by using microcomb with broad chaotic spectrum above 12 GHz. **e**, Velocimetry of the moving target in reciprocating motion at the constant speed of 5.1 mm s<sup>-1</sup>, 9.7 mm s<sup>-1</sup> and 18.9 mm s<sup>-1</sup>, respectively.

shows that all 20 ranging results have a ranging precision of 2 mm, which is the best result among the reported parallel LiDAR systems and one order of magnitude better than the other microcomb-based

LiDAR<sup>8</sup>. Such high distance resolution also has the benefit of distinguishing a moving object in a shorter interval time, which results in better velocity resolution. The velocity measurement was performed

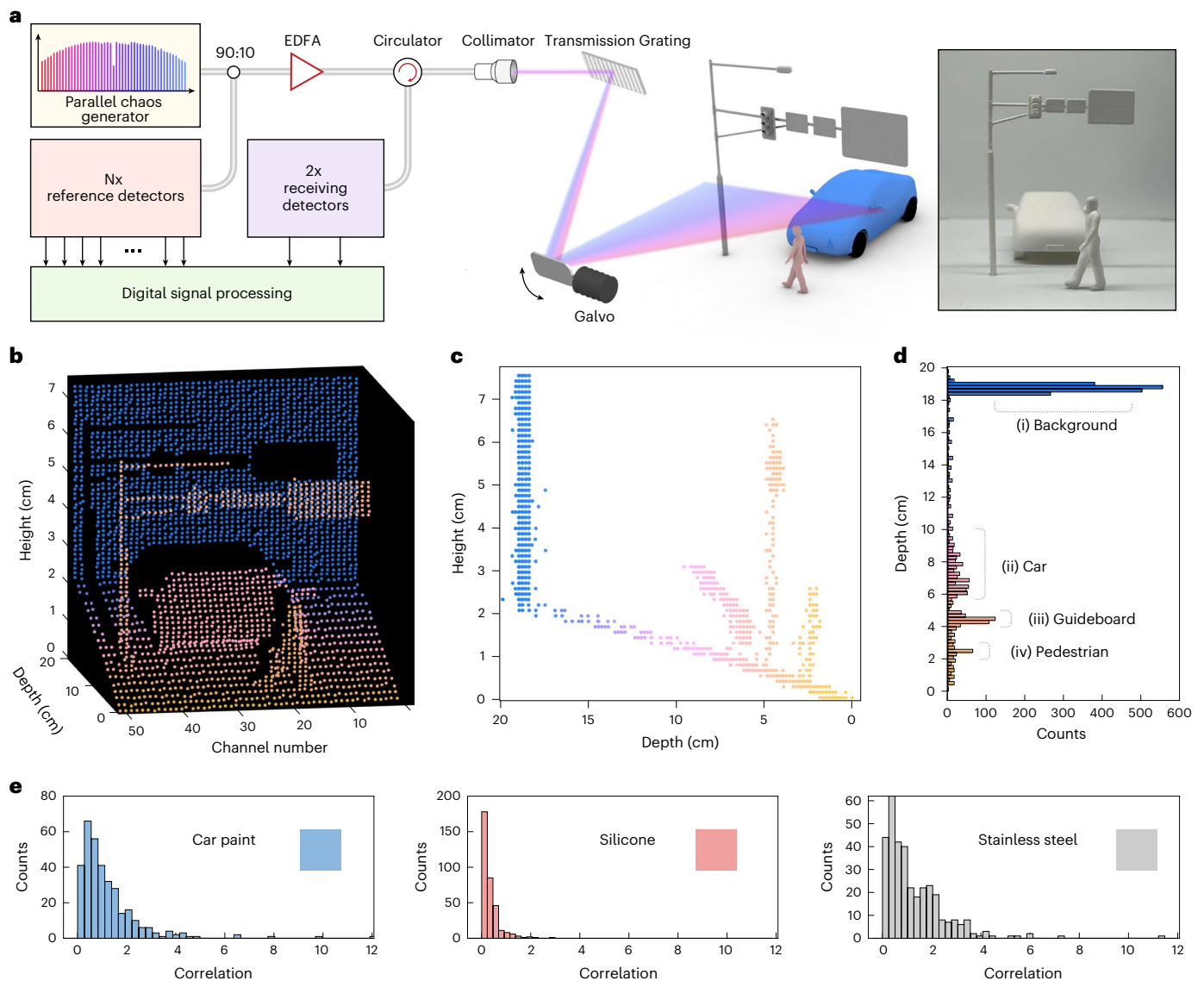


**Fig. 4 | Chaotic comb based parallel 3D imaging.** **a**, Experimental set-up: 51 of the chaotic comb's operational channels were chosen and amplified for 3D imaging. They are dispersed by the transmission grating in the horizontal direction and vertically reflected to different viewpoints through a galvo mirror. The photograph in the inset shows a simulated environment including three objects built to simulate a real detection scenario with a whiteboard background.

**b**, The reconstructed LiDAR imaging frame with 51 pixels in the horizontal scanning line with uniformly spaced samples, and 75 times vertical beam scanning controlled by the galvo mirror. **c,d**, Side-view (**c**) and histogram (**d**) of the LiDAR imaging frame shown in **b**. **e**, The reflectivity detection histograms of the correlation intensity for three cubes with the corresponding materials in the constructed real scene shown in the inset of the **a**.

by ranging a moving object. The target is manipulated in a reciprocating motion at a constant speed on the rail. By continuous measurement, the trajectories of the moving target are recorded at three distinct speeds. As depicted in Fig. 3e, the high ranging precision of the single parallel channel ensures that the low-speed movement can be measured accurately with a resolution of around  $5 \text{ mm s}^{-1}$ , which is limited by the speed restriction of the motorized rail instead of the LiDAR itself.

### Massively parallel 3D imaging

Beyond the great ranging accuracy, we further explore the capability of the chaotic parallel LiDAR by performing high-resolution 3D imaging. Due to the flat-top characteristic of the chaotic microcomb spectrum, a total of 51 distinct comb lines with 90 GHz mode spacing (without the pump) were used for the imaging experiment without an extra filtering process. These detection channels were amplified and mapped to the pixels in the horizontal direction through a transmission

grating. Beam scanning in the vertical direction was performed sequentially through a galvo mirror. A simulated scene containing a model pedestrian, guideboard and a car with 2–3 cm distance spacing was created, and set 1.85 m in front of the collimator (see inset in Fig. 4a). Figure 4b shows the entire  $5.8 \text{ cm} \times 7.6 \text{ cm}$  imaging frame of the reconstructed scene, with a maximum image resolution of  $51 \times 75$  pixels for the static frame. Unlike the previous parallel FMCW LiDAR, whose range resolution and accuracy encountered a degradation caused by the Raman effect and higher-order dispersion<sup>34–36</sup>, the parallel ranging implemented by the chaotic comb overcomes such disadvantages and has consistent range resolution for each operating channel (see Supplementary Note 3). Meanwhile, benefiting from our record-high chaotic spectrum of the comb signal, the three objects in the scene can be clearly distinguished and their recreated shape contours are not distorted, as depicted in Fig. 4c,d. Both the imaging and range resolutions are superior to the parallel ranging results achieved by a previous

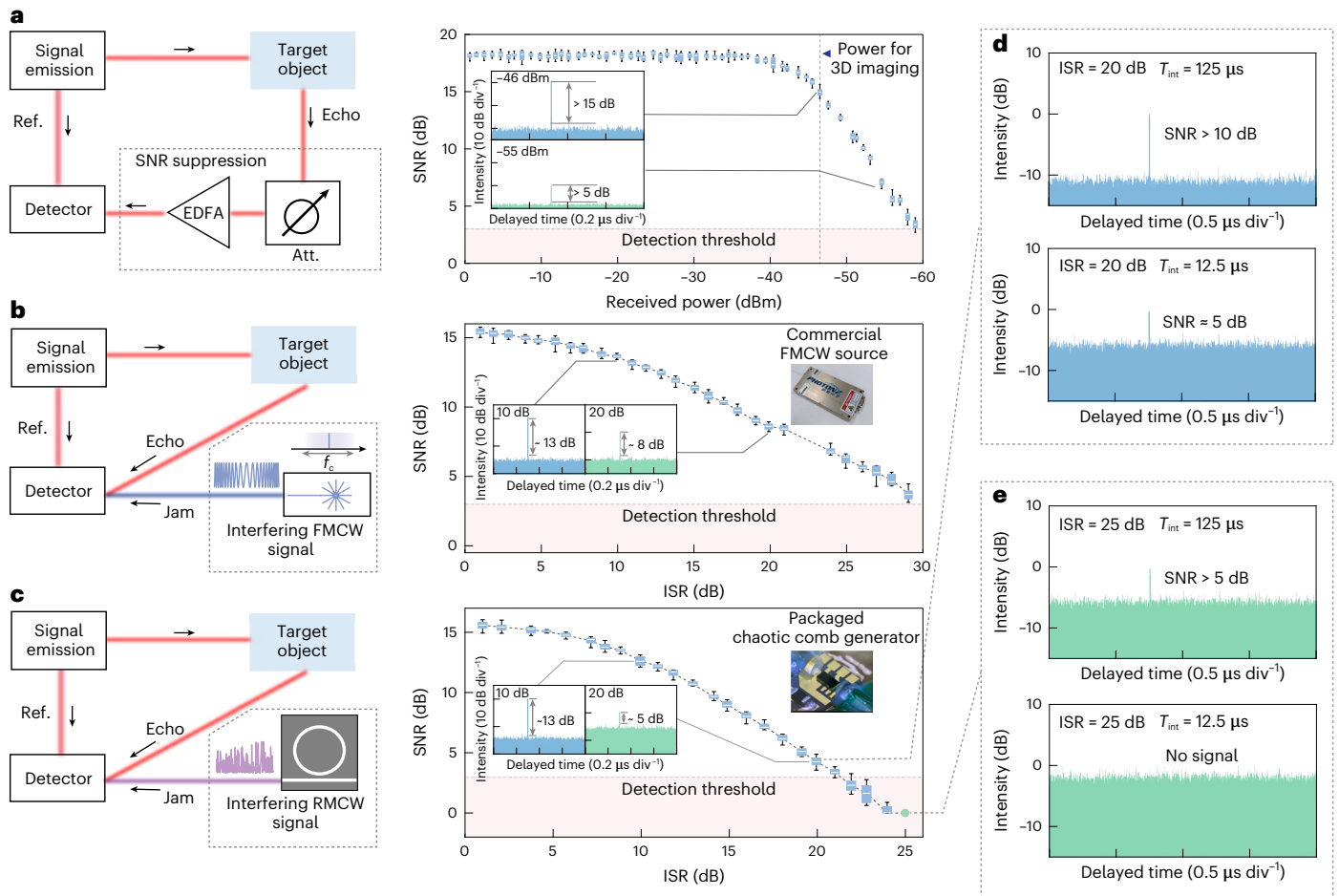


**Fig. 5 | Ranging under several types of interference.** **a**, Ranging with decreased receiving signal power. Left panel: experimental set-up. Right panel: correlation peak SNR with the reduction of received signal power. Inset: correlation results with -46 dBm and -55 dBm received power, respectively. **b,c**, Cross-correlation results under the interference of FMCW (**b**) and RMCW (**c**) signals. Left panels: experimental set-up, where the echo and jam signals are combined by a beam combiner before injection into the detector. Right panels: Correlation peak

SNR with variations of ISR. Inset: correlation results when interference signal intensities are 10 times and 100 times higher than the target echo, respectively. **d,e**, Comparisons of correlation results with an increased integration time of 12.5 μs and 125 μs at receiving end under the ISR of 20 dB (**d**) and 25 dB (**e**). The box plots in **a**, **b** and **c** are derived from the same number of tests ( $N = 10$ ). The horizontal line indicates the median, the box spans 0.25 to 0.75 quartiles and the whisker length corresponds to 1.5 times the interquartile range.

work<sup>8</sup>. To more intuitively demonstrate the range resolution, we also conduct another detection for two sheets of paper with patterns on the front sheet (see Supplementary Note 4). As the accumulation time for each pixel was set to 12.5 μs for better SNR detection, our LiDAR system can achieve a reasonable acquisition rate of 4.1 megapixels per second, which is also comparable to current commercial LiDAR products<sup>37,38</sup>. The effective range for our LiDAR system prototype can be approximately predicted to be 10 m, and the standard deviation of the 3D imaging results is smaller than 2.7 mm (see Supplementary Note 11). The short detection range of our demo system is mainly restricted by the monostatic set-up, whose reflection from the collimator lens does not reduce with increasing distance. A bistatic system can be further considered as it is more flexible to increase the receiving aperture and the reflection from the collimator can be eliminated.

In addition to spatial depth information, the reflectivity is further valuable information extracted from detection. In practical applications, it is mainly used to achieve the preliminary classification of targets with different reflectance for specific target detection such as lane lines while rejecting useless information to assist and accelerate the algorithmic processing of other image-sensing signals. We therefore also performed reflectance detection for the three types of material corresponding to the objects in the created scene, and three cubes with surfaces made of

car paint, silicone and stainless steel were scanned by the same set-up illustrated in Fig. 4a. The intensities of the reflectance were derived from the relative cross-correlation peak intensity relative to the weak reflections of the collimator at each detection point (see Supplementary Note 5 for details). From the histograms of the reflectance detection for each type of material (see Fig. 4e), there is a clear demarcation in the reflection intensity distribution, that is, skin-like materials such as silicone are relatively strong in light absorption, so the intensity of its relative correlation peak value is mostly distributed below 1, whereas the other two materials with stronger scattering are clearly distributed in the interval greater than 2. Although they will also have distributions in the interval with lower relative cross-correlation peaks, this is mainly because the smooth surfaces of these materials are more likely to concentrate light scattering into azimuths far from the receiving aperture of the system.

### Interference-free LiDAR

In the previous section, the orthogonality of the chaotic comb lines eliminates inter-channel interference and simplifies the receiving architecture. Meanwhile, in practical ranging scenarios, the background noises—together with other irrelevant high-intensity signals—will serve as the jamming source, therefore degrading the ranging accuracy or causing fake signals at receiving end. The interference is becoming a severe



problem with the growing popularity of LiDAR in many applications. In spite of that, the microcomb-based parallel chaos proposed here will be invaluable in these applications due to its interference-free capability.

Several experiments are performed in this work to verify such immunity, in which different types of jamming signals (for example, ASE noise (see Supplementary Note 13) and high-power FMCW and randomly modulated continuous wave (RMCW) signals) are intentionally generated and mixed with the echo signal ahead of the receiver, as shown in Fig. 5. The cross-correlations between the mixed receiving and reference signals are then calculated with the variations of the interference–signal ratio (ISR), which refers to the power ratio between the interfering signal and echo signal received at the photodetector. The power proportion between the ASE noise and the target echo in particular is changed by a variable optical attenuator before injection into the erbium-doped fibre amplifier (see Fig. 5a). The result shows a wide detection dynamic range under interference, where flat and saturated SNR of the correlation peaks is maintained when the receiving power is above  $-40$  dBm, before decreasing linearly. The SNR is still beyond the 3 dB detection threshold when the receiving power is attenuated to  $-60$  dBm, much lower than that in the aforementioned 3D imaging experiments, indicating the requirement of laser radiation power could be much lower, which benefits the eye-safe operation.

The interference-free ranging operation is verified by employing intense FMCW and RMCW signals as interfering sources (see Fig. 5b,c). Both results show a correlation peak detectable ISR of larger than 25 dB, which means the interference signal could be resisted even if the detected power is over 200-times higher than that of the target echo signal. It is also worth noting that the SNR degradation here is mainly caused by the reduced signal power rather than interference light as the echo power is deliberately attenuated for the variation of ISR to avoid saturating the receiving photodetector. Moreover, the acceptable ISR could be further improved by increasing the integration time. As shown in Fig. 5d,e, with detection integration time raised from 12.5  $\mu$ s to 125  $\mu$ s, an additional 5 dB correlation peak SNR could be obtained, indicating a  $>30$  dB tolerable ISR. Such an approach provides another dimension for the promotion of receiving SNR compared with traditional detection manners, which favour weak signal detection in extreme conditions.

## Discussion

In summary we have demonstrated a parallel LiDAR that features high-precise ranging and strong jamming immunity. By breaking the temporal and frequency congestion that plagues the conventional parallel schemes, the complexity of the system does not go up as the channel number increases, which is invaluable in practical applications. Without the limitation of channel numbers set by the congestion, the chaotic LiDAR can potentially support massive parallelization with much more channel numbers than current LiDARs. The interference-free nature can allow a high density of devices to work simultaneously. Moreover, the unprecedented ranging accuracy and velocity resolution demonstrated in this work can open many new applications beyond self-driving, such as monitors of small deformation in construction as well as the simultaneous localization and mapping for the rapid-growing metaverse. Although some common problems, such as multi-path interference, can degrade the ranging accuracy of several channels of the parallel chaotic LiDAR, the miniaturization and low-cost properties of our parallel chaotic LiDAR help support multiple LiDAR configurations on a vehicle to scan the overlapped field of view to reduce the influence.

In addition to the performance, the chaotic LiDAR also features a great advantage in terms of cost. The whole system is integration compatible<sup>39</sup>: the DFB laser pump and semiconductor optical amplifiers can be all on an III–V chips or heterogeneous integrated onto silicon-on-insulator technology (ref.<sup>40</sup>) or Si<sub>3</sub>N<sub>4</sub> (ref.<sup>41</sup>), where a solid-state emitter such as OPA<sup>42–45</sup> or FPA<sup>46</sup>, and on-chip highly sensitive APDs<sup>47</sup> have been already demonstrated. As such, the entire system can be massively produced at a wafer scale by photonic foundries,

which will considerably accelerate the spreading of the technology in the consumer market.

Furthermore, the chaotic microcomb source can also play key roles in a much broader scope beyond what we demonstrated here. As the modulation instability state also features random frequency modulation<sup>48</sup>, the heterodyne detection scheme<sup>49</sup> is a feasible manner to use another soliton state microcomb with identical mode spacing as the local oscillators, which features advantages in long-range detection and instant multidimensional perception capability, although at the expense of hardware complexity. Importantly, such parallel chaos can be transferred to other electromagnetic frequencies through frequency division multiplexing, therefore benefiting radar, millimetre-wave and terahertz sensing, and so on. This work opens a window for the active use of modulation instability comb, which has been paid little attention before compared with its counterparts of coherent states like bright solitons<sup>27,50–53</sup> and dark pulse solitons<sup>54–56</sup>. With many desirable properties, such a special light source can lead to a profound impact on many other applications, such as random number generation<sup>57</sup> and communication<sup>58</sup>.

## Online content

Any methods, additional references, Nature Portfolio reporting summaries, source data, extended data, supplementary information, acknowledgements, peer review information; details of author contributions and competing interests; and statements of data and code availability are available at <https://doi.org/10.1038/s41566-023-01158-4>.

## References

- Kim, I. et al. Nanophotonics for light detection and ranging technology. *Nat. Nanotechnol.* **16**, 508–52456 (2021).
- Lidar drives forwards. *Nat. Photon.* **12**, 441 (2018).
- Na, Y. et al. Ultrafast, sub-nanometre-precision and multifunctional time-of-flight detection. *Nat. Photon.* **14**, 355–360 (2020).
- Mahjoubfar, A. et al. Time stretch and its applications. *Nat. Photon.* **11**, 341–351 (2017).
- Liu, J., Sun, Q., Fan, Z. & Jia, Y. TOF lidar development in autonomous vehicle. In *2018 IEEE 3rd Optoelectronics Global Conference (OGC)* 185–190 (IEEE, 2018).
- HESAI AT128 Product (HESAI, accessed 12 Mar 2023); <http://www.hesaitech.com/product/at128/>
- Diehm, A. L., Hammer, M., Hebel, M. & Arens, M. Mitigation of crosstalk effects in multi-lidar configurations. In *Electro-Optical Remote Sensing XII*, **10796**, 1079604 (International Society for Optics and Photonics, 2018).
- Riemensberger, J. et al. Massively parallel coherent laser ranging using a soliton microcomb. *Nature* **581**, 164–170 (2020).
- Hwang, I.-P. & Lee, C.-H. Mutual interferences of a true-random lidar with other lidar signals. *IEEE Access* **8**, 124123–124133 (2020).
- Abu-Rgheff, M. A. *Introduction to CDMA Wireless Communications* (Academic, 2007).
- Rabideau, D. J. & Parker, P. Ubiquitous MIMO multi-function digital array radar. In *37th Asilomar Conference on Signals, Systems and Computers* Vol. 1, 1057–1064 (IEEE, 2003).
- Chen, C.-Y. & Vaidyanathan, P. MIMO radar ambiguity properties and optimization using frequency-hopping waveforms. *IEEE Trans. Signal Process.* **56**, 5926–5936 (2008).
- Sturm, C., Sit, Y. L., Braun, M. & Zwick, T. Spectrally interleaved multi-carrier signals for radar network applications and multi-input multi-output radar. *IET Radar, Sonar Navig.* **7**, 261–269 (2013).
- Chung, F. R., Salehi, J. A. & Wei, V. K. Optical orthogonal codes: design, analysis and applications. *IEEE Trans. Inf. Theory* **35**, 595–604 (1989).
- Kim, G. & Park, Y. Lidar pulse coding for high resolution range imaging at improved refresh rate. *Opt. Express* **24**, 23810–23828 (2016).



16. Fersch, T., Weigel, R. & Koelpin, A. A CDMA modulation technique for automotive time-of-flight lidar systems. *IEEE Sens. J.* **17**, 3507–3516 (2017).
17. Tsai, C.-M. & Liu, Y.-C. Anti-interference single-photon lidar using stochastic pulse position modulation. *Opt. Lett.* **45**, 439–442 (2020).
18. Feng, L. et al. FPGA-based digital chaotic anti-interference lidar system. *Opt. Express* **29**, 719–728 (2021).
19. Lin, F.-Y. & Liu, J.-M. Chaotic lidar. *IEEE J. Sel. Top. Quantum Electron.* **10**, 991–997 (2004).
20. Wang, B., Wang, Y., Kong, L. & Wang, A. Multi-target real-time ranging with chaotic laser radar. *Chin. Opt. Lett.* **6**, 868–870 (2008).
21. Wang, B., Zhao, T. & Wang, H. Improvement of signal-to-noise ratio in chaotic laser radar based on algorithm implementation. *Chin. Opt. Lett.* **10**, 052801 (2012).
22. Zhong, D., Xu, G., Luo, W. & Xiao, Z. Real-time multi-target ranging based on chaotic polarization laser radars in the drive-response vcsels. *Opt. Express* **25**, 21684–21704 (2017).
23. Chen, J.-D., Wu, K.-W., Ho, H.-L., Lee, C.-T. & Lin, F.-Y. 3-D multi-input multi-output (MIMO) pulsed chaos lidar based on time-division multiplexing. *IEEE J. Sel. Top. Quantum Electron.* **28**, 1–9 (2022).
24. Axelsson, S. R. Noise radar using random phase and frequency modulation. *IEEE Trans. Geosci. Remote Sens.* **42**, 2370–2384 (2004).
25. Chang, L. et al. Ultra-efficient frequency comb generation in algaas-on-insulator microresonators. *Nat. Commun.* **11**, 1331 (2020).
26. Xie, W. et al. Ultrahigh-Q AlGaAs-on-insulator microresonators for integrated nonlinear photonics. *Opt. Express* **28**, 32894–32906 (2020).
27. Kippenberg, T. J., Gaeta, A. L., Lipson, M. & Gorodetsky, M. L. Dissipative kerr solitons in optical microresonators. *Science* **361**, 567 (2018).
28. Takeuchi, N., Sugimoto, N., Baba, H. & Sakurai, K. Random modulation CW lidar. *Appl. Opt.* **22**, 1382–1386 (1983).
29. Carmon, T., Yang, L. & Vahala, K. J. Dynamical thermal behavior and thermal self-stability of microcavities. *Opt. Express* **12**, 4742–4750 (2004).
30. Li, Q. et al. Stably accessing octave-spanning microresonator frequency combs in the soliton regime. *Optica* **4**, 193–203 (2017).
31. Lukashchuk, A., Riemensberger, J., Karpov, M., Liu, J. & Kippenberg, T. J. Dual chirped micro-comb based parallel ranging at megapixel-line rates. *Nat. Commun.* **13**, 1–8 (2022).
32. Jiang, Y., Karpf, S. & Jalali, B. Time-stretch lidar as a spectrally scanned time-of-flight ranging camera. *Nat. Photon.* **14**, 14–18 (2020).
33. Zang, Z. et al. Ultrafast parallel single-pixel lidar with all-optical spectro-temporal encoding. *APL Photon.* **7**, 046102 (2022).
34. Karpov, M. et al. Raman self-frequency shift of dissipative kerr solitons in an optical microresonator. *Phys. Rev. Lett.* **116**, 103902 (2016).
35. Cherenkov, A. V., Lobanov, V. E. & Gorodetsky, M. L. Dissipative kerr solitons and cherenkov radiation in optical microresonators with third-order dispersion. *Phys. Rev. A* **95**, 033810 (2017).
36. Yi, X. et al. Single-mode dispersive waves and soliton microcomb dynamics. *Nat. Commun.* **8**, 14869 (2017).
37. Aeva Series Product (accessed 20 Jan 2022); <https://www.aeva.com/>
38. Hesai Pandar128 Product (accessed 20 Jan 2022); <https://www.hesaitech.com/zh/Pandar128>
39. Shu, H. et al. Microcomb-driven silicon photonic systems. *Nature* **605**, 457–463 (2021).
40. Davenport, M. L. et al. Heterogeneous silicon/iii-v semiconductor optical amplifiers. *IEEE J. Sel. Top. Quantum Electron.* **22**, 78–88 (2016).
41. Tran, M. et al. Extending the spectrum of fully integrated photonics to submicrometre wavelengths. *Nature* **610**, 54–60 (2022).
42. Sun, J., Timurdogan, E., Yaacobi, A., Hosseini, E. S. & Watts, M. R. Large-scale nanophotonic phased array. *Nature* **493**, 195–199 (2013).
43. Hutchison, D. N. et al. High-resolution aliasing-free optical beam steering. *Optica* **3**, 887–890 (2016).
44. Poulton, C. V. et al. 8192-element optical phased array with 100° steering range and flip-chip CMOS. In *2020 Conference on Lasers and Electro-Optics JTh4A-3* (Optical Society of America, 2020).
45. Miller, S. A. et al. Large-scale optical phased array using a low-power multi-pass silicon photonic platform. *Optica* **7**, 3–6 (2020).
46. Rogers, C. et al. A universal 3D imaging sensor on a silicon photonics platform. *Nature* **590**, 256–261 (2021).
47. Masahiro, N., Toshihide, Y., Fumito, N., Hideaki, M. & Kimikazu, S. High-speed avalanche photodiodes toward 100-gbit/s per lambda era. *NTT Technical Rev.* **16**, 45–51 (2018).
48. Herr, T. et al. Universal formation dynamics and noise of kerr-frequency combs in microresonators. *Nat. Photonics* **6**, 480–487 (2012).
49. Lukashchuk, A., Riemensberger, J., Tusnín, A., Liu, J. & Kippenberg, T. Chaotic micro-comb based parallel ranging. Preprint at <https://arxiv.org/abs/2112.10241> (2021).
50. Stern, B., Ji, X., Okawachi, Y., Gaeta, A. L. & Lipson, M. Battery-operated integrated frequency comb generator. *Nature* **562**, 401–405 (2018).
51. Xiang, C. et al. Laser soliton microcombs heterogeneously integrated on silicon. *Science* **373**, 99–103 (2021).
52. Chang, L., Liu, S. & Bowers, J.E. Integrated optical frequency comb technologies. *Nat. Photon.* **16**, 95–108 (2022).
53. Shen, B. et al. Integrated turnkey soliton microcombs. *Nature* **582**, 365–369 (2020).
54. Xue, X. et al. Mode-locked dark pulse Kerr combs in normal-dispersion microresonators. *Nat. Photon.* **9**, 594–600 (2015).
55. Shu, H. et al. Sub-milliwatt, widely-tunable coherent microcomb generation with feedback-free operation. Preprint at <https://arxiv.org/abs/2112.08904> (2021).
56. Jin, W. et al. Hertz-linewidth semiconductor lasers using CMOS-ready ultra-high-Q microresonators. *Nat. Photon.* **15**, 346–353 (2021).
57. Kim, K. et al. Massively parallel ultrafast random bit generation with a chip-scale laser. *Science* **371**, 948–952 (2021).
58. Vanwiggeren, G. D. & Roy, R. Communication with chaotic lasers. *Science* **279**, 1198–1200 (1998).

**Publisher's note** Springer Nature remains neutral with regard to jurisdictional claims in published maps and institutional affiliations.

**Open Access** This article is licensed under a Creative Commons Attribution 4.0 International License, which permits use, sharing, adaptation, distribution and reproduction in any medium or format, as long as you give appropriate credit to the original author(s) and the source, provide a link to the Creative Commons license, and indicate if changes were made. The images or other third party material in this article are included in the article's Creative Commons license, unless indicated otherwise in a credit line to the material. If material is not included in the article's Creative Commons license and your intended use is not permitted by statutory regulation or exceeds the permitted use, you will need to obtain permission directly from the copyright holder. To view a copy of this license, visit <http://creativecommons.org/licenses/by/4.0/>.

© The Author(s) 2023

## Methods

### Fabrication and characterization of the chaotic source

The microresonators were fabricated by heterogeneous wafer bonding. The AlGaAs epitaxial films were grown by molecular-beam epitaxy. A 248 nm deep-ultraviolet stepper was used for the lithography. A photoresist reflow process and an optimized dry etch process were applied in waveguide patterning for waveguide scattering loss reduction. The Q-factor for the 90 GHz and 1 THz rings are around 1.5 million and 1 million, respectively. An inverse taper, with the waveguide width adiabatically narrowed from 600 to 200 nm, was used here for efficient chip-to-fibre coupling with a transverse electric fundamental mode; the coupling loss is -3 dB per facet.

The chaotic microcombs were generated via manually tuning an external-cavity-diode laser (Toptica CTL 1550) from the blue detuning side into the resonance. To promote the chaotic spectrum, the pump was amplified by an erbium-doped fibre amplifier for power boosting to around 200 mW. By improving the coupling efficiency and using an over-coupled state, the actual requirement for optical power amplification can be further reduced to meet the capability of existing on-chip semiconductor optical amplifiers<sup>40</sup>, which is of great significance for hybrid integration of the continuous-wave laser and microring resonator. Furthermore, defective modes in the photonic crystal microring can greatly reduce the mode volume<sup>59</sup>, potentially allowing for greater nonlinear effects at a lower power and higher chaotic spectrum. A bandpass filter was then used to filter out the broadband ASE noise. The microcomb spectra are recorded by an optical spectrum analyser (Yokogawa AQ6370C). For the autocorrelation test, each single comb line is selected by an optical spectral shaper (Finisar Waveshaper 4000 S) with its programmatic interface. The time domain waveform of each chaotic channel was then recorded by a real-time oscilloscope (Keysight UXR0334A) for further data analysis. The radio frequency spectrum of the microcomb is measured by an Electrical Spectrum Analyzer (Keysight N9010BU), with a resolution bandwidth of 100 kHz.

### Experimental details

For distance and velocity measurement, a single comb line is selected as the operating channel, where, particularly, an 850 GHz chaotic comb is employed for high-accuracy characterization. After optical amplification, the power splitter separates 90% power into the signal path and the residual power into the photodetector (Finisar XPDV2150R) as a reference. Then the signal was launched into free space by a fibre optic collimator with a waist diameter of 4.65 mm to probe the whiteboard that is mounted on a programmable motorized slide rail. The echo signal was collected by the same collimator and then sent to the receiver after amplification. A lens with a focal length of 750 mm was placed between the collimator and whiteboard for a larger receiving aperture. Each distance step in the static test is carefully calibrated, and real-time surveying is performed for velocity extraction. As our measurement is based on the continuous wave, the clock and time jitter of the data sampling will not change the stochastic properties of the signal. The time interval between two ranging samples is realized by controlling the oscilloscope sampling with code, so high clock accuracy can be ensured for good velocity resolution.

For 3D imaging, we employ the monostatic detection scheme for proof-of-principle parallel detection. The experimental set-up is depicted in Fig. 4a, in which comb generation and receiving units are presented in a simplified way. The chaotic channels are horizontally dispersed by a 966 lines per millimetre transmission grating, refracted into the vertical direction by a 45° mirror, and then guided to the galvo (Thorlab QS45Y-AG) for vertical scanning. The optimal incident angle of the transmitted comb lines is 48.3° (perpendicular to the grating), and each channel can realize maximum power transmission into the first diffraction order. The choice of grating parameters must be related to the field of view requirements, and a larger field of view needs a comprehensive consideration of channel spacing (free spectral range),

spectrum range and the angular dispersion of the diffraction components. The detection targets (spaced at about 2–3 cm) are all placed on a slightly angled plate with a background board set behind. The distance between the collimator and targets is about 1.85 m, with a 1,000 mm focal length lens setting behind the grating. The targets we use for reflectivity detection are three cubes with surfaces made of silicone, car paint, and stainless steel. They are embedded in three vertically aligned holes in a whiteboard, and the number of detection points is set up to 306 (18 × 17) on each of their surfaces.

For anti-interference characterization, a single chaotic comb line is selected and emitted toward the target object. The echo signals are then collected and combined with the jamming signal by a fibre-based beam combiner. The mixed signals are amplified by a pre-amplifier before injection into the photodetector. The amplifier could be further removed from the system by using high-gain avalanche photodiodes. A commercial FMCW source (PhotonX laser) and an RMCW source from another packaged AlGaAs sample, generating a chaotic comb with 90 GHz mode spacing, serve as the jamming signal, respectively. An optical attenuator is employed after the interference signal for ISR adjustment.

### Numerical simulation

To compare chaotic combs generated in different integrated nonlinear platforms, simulations based on the Lugiato–Lefever equation

$$\epsilon_R \frac{\partial E(t, \tau)}{\partial t} = \left[ -\left(\frac{\alpha}{2} - i\delta_0\right) + iL \sum_{k \geq 1} \frac{\beta_k}{k!} \left(i \frac{\partial}{\partial \tau}\right)^k \right] E + iLY|E|^2 E + \sqrt{\theta} E_{in} \quad (3)$$

are performed with parameters reported in refs.<sup>60–63</sup>;  $E(t, \tau)$  represents the intracavity optical field;  $E_{in}$  is the pump optical field;  $\alpha$  indicates the loss coefficient;  $\theta$  is the coupling coefficient;  $\delta_0$  is the detuning between the pump laser and the cold cavity resonance;  $\beta_k$  is the  $k$ -order dispersion;  $\epsilon_R$  and  $L$  are the round-trip time and round-trip length of the microcavity, respectively. The Lugiato–Lefever equation is solved based on the Runge–Kutta method. In the simulation, the pump laser is swept into the resonance from a lower frequency and stopped before the intracavity state drop to the continuous-wave state. The intracavity field evolution for 1 million round-trip times is recorded and employed to estimate the FWHM of each comb line. Under a certain parameter group, the largest FWHM for all comb lines is recorded to characterize the chaotic dynamic. Details can be found in Supplementary Note I.

### Data availability

The data that supports the plots within this paper and other findings of this study are available on Zenodo (<https://doi.org/10.5281/zenodo.7401674>). All other data used in this study are available from the corresponding authors on reasonable request.

### Code availability

The codes that support the findings of this study are available from the corresponding authors on reasonable request.

### References

- Lu, X., McClung, A. & Srinivasan, K. High-Q slow light and its localization in a photonic crystal microring. *Nat. Photon.* **16**, 66–71 (2022).
- Liu, X. et al. Aluminum nitride nanophotonics for beyond-octave soliton microcomb generation and self-referencing. *Nat. Commun.* **12**, 1–7 (2021).
- Zheng, Y. et al. Integrated gallium nitride nonlinear photonics. *Laser Photon. Rev.* **16**, 2100071 (2022).
- Guidry, M. A., Lukin, D. M., Yang, K. Y., Trivedi, R. & Vučković, J. Quantum optics of soliton microcombs. *Nat. Photon.* **16**, 52–58 (2022).

63. Liu, J. et al. High-yield, wafer-scale fabrication of ultralow-loss, dispersion-engineered silicon nitride photonic circuits. *Nat. Commun.* **12**, 1–9 (2021).

## Acknowledgements

We thank H. Chen and X. Zhu for fruitful discussions, T. J. Morin for helpful comments on the paper, F. Yang, Z. Ge, Y. Zhou in Peking University Yangtze Delta Institute of Optoelectronics for packaging support, and Shenzhen PhotonX Technology Company for offering the FMCW laser. The UCSB nano-fabrication facility was used.

## Author contributions

The idea was conceived by R.C. and H.S. The experiments were conceived by R.C., H.S., B.S. and L.C. The AlGaAsOI microresonators were designed by H.S. and L.C. The microcomb simulation and modeling are conducted by B.S. Ranging experiments were conducted by R.C., H.S. and B.S. with the assistance of W.L. and Z.T. The AlGaAsOI microresonators were fabricated by W.X. and L.C. The results are analysed by B.S. and R.C. All of the authors participated in

writing the paper. The project was performed under the supervision of L.C., J.E.B., and X.W.

## Competing interests

The authors declare no competing interests.

## Additional information

**Supplementary information** The online version contains supplementary material available at <https://doi.org/10.1038/s41566-023-01158-4>.

**Correspondence and requests for materials** should be addressed to Lin Chang, John E. Bowers or Xingjun Wang.

**Peer review information** *Nature Photonics* thanks Mingjiang Zhang and the other, anonymous, reviewer(s) for their contribution to the peer review of this work.

**Reprints and permissions information** is available at [www.nature.com/reprints](http://www.nature.com/reprints).